A Comparative Study of Alternative Algorithms for Synchrophasor Estimation and Grid Synchronization

Atul Singh, *Member, IEEE*, David Macii, *Senior Member, IEEE*, Dario Petri, *Fellow, IEEE*

Abstract

A critical challenge for the evolution of smart distribution systems is the shortage of measurement devices, along with the complexity and the high costs for deploying new fine-grained monitoring infrastructures. To address this issue, this paper investigates the feasibility of upgrading the grid synchronization algorithms running in the control unit of grid-following power converters to turn them into auxiliary embedded measurement devices supporting system observability. This goal can be achieved in two alternative ways: either by using an algorithm originally designed for a Phasor Measurement Unit (PMU) to perform grid synchronization or, conversely, by applying a grid synchronization technique for synchrophasor estimation. To compare advantages and disadvantages of either approach, both a 2-stage Tuned Lightweight version of the Taylor-Fourier Transform (2-stage TLTFT) algorithm and a Phase-Locked Loop embedding a custom Third-Order Generalized Integrator (TOGI-PLL) are analyzed both in the P Class PMU testing conditions specified in the IEEE Standard IEC/IEEE 60255-118-1:2018 and considering the requirements for grid connection reported in the IEEE Standard 1547-2023. Extensive simulation results show that the general idea of a joint solution for synchrophasor estimation and grid synchronization is viable in either way, although some improvement is needed. In particular, the 2-stage TLTFT algorithm generally returns more accurate results and shorter response times than the TOGI-PLL, but it is also more computationally demanding. Further simulations, based on a real power electronic converter model, confirm that, when either algorithm is used in the control loop for grid synchronization, the generated output voltage is stable.

Keywords

Phasor Measurement Units (PMU); Phase-Locked Loops (PLL); Grid-Following Power Converters; Grid synchronization; Performance evaluation.

I. Introduction

The current and future proliferation of electric vehicles, Distributed Energy Resources (DERs) is expected to cause increasing hosting capacity problems of renewable-based (e.g. Photovoltaic – PV) generators [1], as well as strongly time-varying power demand and supply fluctuations that could undermine grid stability, unless they are mitigated by strategies that better align generation and consumption profiles [2].

Such problems can be reduced through advanced and flexible power flow control techniques, possibly involving energy communities [3], [4]. However, such techniques require estimating the state of a distribution system in real-time and with high accuracy [5]. Unfortunately, this is a well-recognized challenge for smart grids due to the economic and infrastructural constraints that limits the wide scale deployment of high-accuracy, high-rate measurement devices, such as the Phasor Measurement Units (PMUs) [6], [7]. The limited distribution systems observability due to the shortage of measurement points can be easily addressed using virtual measurements (e.g., zero power injections at buses without loads) or pseudo-measurements (e.g., based on aggregated historical active and reactive power data) [8]. However, this approach comes at the cost of reduced state estimation accuracy, particularly under highly dynamic operating conditions [9].

To improve state estimation capability and performance, two complementary approaches exist. The most obvious one is to place high-rate, high-accuracy synchronized instruments like the PMUs in strategic points of the distribution system to maximize observability, while minimizing deployment costs [10]–[13]. Alternatively, the grid measurement and monitoring capabilities can be enhanced by leveraging or upgrading existing devices, most notably those of the Advanced Metering Infrastructure (AMI) [14]–[17].

An emerging approach, that somehow extends the previous one, concerns with upgrading other existing devices to insert additional measurement points into the grid, thereby improving system observability. An interesting example of this idea is reported in [18], where the data collected from both smart inverters of PV generators and weather stations are merged with the measurement data typically used for distribution system state estimation. Furthermore, it is shown in [19] that state estimators relying on PV generation data and further supported by PMUs installed near the buses with the highest PV penetration, achieve higher accuracy than conventional state estimation techniques. The aforementioned results suggest that if the Power Electronic Converters (PECs) were instrumented to measure one or more electrical quantities, at the point of common coupling, system observability could be enhanced significantly. With reference to the EU regulation establishing a network code on requirements

Atul Singh, David Macii and Dario Petri are with the Department of Industrial Engineering of the University of Trento, Via Sommarive, 9 Trento, Italy, 38123. The corresponding Author is David Macii: david.macii@unitn.it.

This work was funded by the European Union - Next Generation EU, Mission 4, Component 2, through the Italian Ministerial grant PRIN 2022 “Smart grid-connected power converters based on advanced synchrophasor-inspired harmonics measurements for holistic integration of renewable energy sources (POWERHERO),” n. 20224X2AYH, CUP F53D23000490006.

for grid connection of generators [20], the PMU-like measurement functions could be integrated into the control units of Medium-Voltage (MV), grid-following converters of power park modules of Type B or C with installed capacity ranging from about 1 MW up to some tens of MW.

Considering that the number of PECs is expected to steadily grow in future as a result of the increasing penetration of renewable energy sources and energy communities [4], the idea of embedding measurement functions into the PECs' control units to turn them into auxiliary instruments for grid monitoring using a few additional hardware and software resources deserves to be investigated in depth for the reasons listed below, i.e.,

- PECs' control units already include several ancillary functions such as, for instance, volt/var optimization, active power flow management, and last but not least, local power quality monitoring [21]. For this reason, the Root Mean Square (RMS) amplitude of AC voltage and current waveforms, voltage frequency on the Electric Power System (EPS) side, as well as active and reactive power and Total Harmonic Distortion (THD) are already measured locally, usually at a low rate to support the connection of DERs to the EPS.
- DER interconnection and interoperability must meet tight grid synchronization requirements that are achieved through various techniques, usually based on Phase-Locked Loops (PLLs) [22]. Interestingly, some PMU prototypes also rely on a PLLs [23], [24]. Even though the performance requirements in either case are usually rather different, the fact that in both kinds of applications a PLL-based architecture is suitable, suggests that a device addressing both problems at the same time could be designed, provided that a Coordinated Universal Time (UTC) reference is connected to the PEC control unit. Such a reference can be provided not only by Global Positioning Systems (GPS) receivers, but also by the Precision Time Protocol (PTP), particularly if the IEEE C37.238-2017 standard profile for power system applications is used [25], [26].
- Finally, it is important to note that smart PECs should not be regarded as standalone devices. In the future, they are expected to communicate and cooperate to enhance grid resilience and stability [27]. Therefore, these devices will likely be equipped with networking capabilities, which could be used to gather and share measurement data as well.

Of course, even if both the PMU and the grid synchronization algorithms have to measure the RMS value, the instant phase and the frequency of AC voltage waveforms, some fundamental differences also exist. In the PMU case, such parameters (along with the Rate of Change of Frequency – ROCOF) must be timestamped at instants synchronized to UTC before they are transferred to the Phasor Data Concentrator (PDC) at a given reporting rate, which is typically an integer multiple of the fundamental period.

The grid synchronization techniques for grid-following PECs are instead normally used just locally to control the connection of the PEC output waveform to the EPS, with no need for UTC time-stamping or remote data reporting.

To the best of authors' knowledge, only another research on a similar subject was conducted in the recent past [28]. That work presents a controller prototype for PV inverters providing both reactive power control and PMU functionality. However, the concept of using a single algorithm for joint synchrophasor estimation and grid synchronization remains largely unexplored. This raises the fundamental question of whether it is more effective to use a PMU algorithm for grid synchronization, or to employ a grid synchronization technique for synchrophasor estimation. Thus, the objective of this paper is to investigate this problem by extending the preliminary results presented in [29]. In particular, while in [29] a synchrophasor estimation algorithm was tested to check if it can meet the grid synchronization requirements for DER connection reported the IEEE Standard 1547-2023 [30], in this paper the performance of a PLL originally designed for grid synchronization and subsequently enhanced to improve estimation accuracy is also analyzed under the P Class PMU testing conditions (i.e., for protection purposes) reported in the IEC/IEEE Standard 60255-118-1:2018 [31].

The rest of the paper is structured as follows. First, in Section II, both algorithms and the related theoretical background are described. Since the PLL is inherently designed to process three-phase sinusoidal signals, the PMU algorithm proposed in [29] has also been adapted to operate in a three-phase framework to enable a fair comparison. In Section III, after a brief discussion on algorithms' settings, the considered techniques are characterized both in the P Class PMU testing conditions specified in [31], and considering the DER connection requirements of [30]. Then, in Section IV, both algorithms under test are replaced to the standard Synchronous Reference Frame (SRF) PLL of a real grid-following PEC model to check the overall closed-loop stability and performance in realistic operating conditions. Finally, Section V concludes the paper and briefly outlines the future work.

II. Algorithms Description

As briefly introduced in Section I, the algorithms considered in this paper have inherently a different origin. The first one is called two-stage Tuned Lightweight Taylor-Fourier Transform (2-stage TLTFT for brevity) and it is described in Section II-A.

The second algorithm belongs instead to a category of methods that are more commonly used for grid synchronization, namely a Third-Order Generalized Integrator Phase-Locked Loop (TOGI-PLL), which is explained in Section II-B).

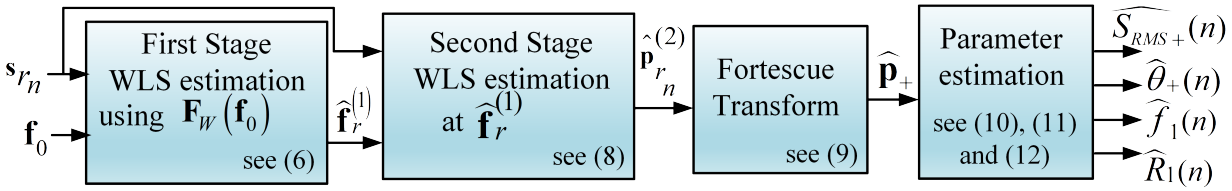

Fig. 1. Block diagram of the 2-stage TLTFT algorithm.

In both cases, the acquired waveform is supposed to be a three-phase signal consisting of terms

$$\begin{aligned} s_1(t) &= \sum_{h=1}^{H} S_{1_h}(t)\cos\left(2\pi f_h t + \theta_{1_h}(t)\right), \\ s_2(t) &= \sum_{h=1}^{H} S_{2_h}(t)\cos\left(2\pi f_h t + \theta_{2_h}(t) - \frac{2}{3}\pi\right), \\ s_3(t) &= \sum_{h=1}^{H} S_{3_h}(t)\cos\left(2\pi f_h t + \theta_{3_h}(t) - \frac{4}{3}\pi\right), \end{aligned} \tag{1}$$

where $S_{1_h}(t)$, $S_{2_h}(t)$ and $S_{3_h}(t)$ denote the amplitudes of the $h-$th harmonic of each three-phase component; $\theta_{1_h}(t)$, $\theta_{2_h}(t)$ and $\theta_{3_h}(t)$ represent the respective phasor angles at time t and f_h is the frequency of the $h-$th harmonic. Note that in (1) the magnitude and phase of all harmonic phasors are assumed to be time-varying quantities. In the rest of this paper, synchrophasor magnitude and phase, as well as signal frequency and ROCOF are assumed to be estimated from the positive sequence only of (1), in line with other solutions reported in the technical literature [32]. Also, the signals in (1) are acquired and processed with sampling rate f_s, which is supposed to be an integer multiple of the fundamental nominal frequency f_0 (i.e., 50 Hz or 60 Hz).

A. Two-stage Tuned Lightweight Taylor-Fourier Transform

The 2-stage TLTFT algorithm is designed to estimate the coefficients of the fundamental phasor as well as a limited number of harmonic phasors through a weighted least-squares estimator that processes the samples of data records of fixed duration T. To the best of the authors' knowledge, this approach was first introduced for fundamental synchrophasor estimation in [33] and later extended to handle multiple harmonics in [34]. However, both versions present two main limitations. They are sensitive to off-nominal frequency deviations (since the system matrix elements are computed assuming nominal frequency) and the computational load may become excessive. Specifically, while the basic estimator in [33] is strongly affected by harmonics, the extended formulation in [34], which includes the Taylor-series coefficients of all harmonics of interest, is too computationally intensive for PEC grid synchronization. Other techniques based on similar estimators, but conceived to improve synchrophasor accuracy through preliminary harmonics whitening [35] or narrowband interferer detection [36], are likewise unsuitable for grid synchronization, or whenever sub-millisecond execution is required. To address these issues, the 2-stage TLTFT algorithm described in the following relies on the same lightweight strategy explained in [37], but with some improvement. In particular, the preliminary stage for fundamental-frequency estimation based on a band-pass filter followed by either an Interpolated DFT (IpDFT) [37] or Zero-Crossing Detection (ZCD) [38], is here replaced by a least-squares TFT estimator, in which the pseudo-inverse matrix coefficients are precomputed and stored in memory, to minimize runtime operations.

The block diagram of the resulting 2-stage TLTFT algorithm is depicted in Fig. 1. Compared with the standard TFT, three key enhancements are applied, i.e.,

1) The Kaiser window is used to weight the raw sample data within each observation interval. Indeed, this parametric windows allows a fine-tuning of the spectral main-lobe width relative to the side-lobe levels, thereby keeping the effect of spectral leakage under tight control [38].
2) The data records consist of just two nominal cycles at a time. This length minimizes the computational load of the algorithm ensuring good accuracy even under the effect of a significant harmonic distortion [37]. Moreover, it is shown in [37] that when two-cycle-long data records are used, including more than four harmonics in the TFT model does not further significantly improve estimation accuracy.
3) Finally, the algorithm is computed twice, first assuming that the waveform fundamental frequency equals its nominal value, and then using the actual frequency estimate resulting from the first step. This choice strongly mitigates the effect of possible off-nominal frequency deviations, and it also ensures a better estimation of the harmonic components, thus attenuating their impact on fundamental phasor estimation.

Let $N \approx T f_s$ be the number of samples in each data record. Following the same approach described in [34], if the dynamic phasor of the $h-$th harmonic of phase $r = \{1,2,3\}$ is described by its Taylor's series centered at time $t_c = \frac{n}{f_s}$ and truncated to order K_h (for $h = 1, \ldots, H$), the discrete-time signal model (1) can be rewritten as

$$\begin{aligned} s_r(t) = & \sum_{h=1}^{H} \frac{1}{2} \left[p_{r_h}(t)\, e^{j2\pi f_h t} + \overline{p}_{r_h}(t)\, e^{-j2\pi f_h t} \right] \approx \\ \approx & \frac{1}{2} \sum_{h=1}^{H} \left[\left(\sum_{k=0}^{K_h} \frac{p_{r_{h,k}}(n)}{f_s^k k!} \ell^k \right) e^{j2\pi \frac{f_h}{f_s}(n+\ell)} + \right. \\ & \left. \left(\sum_{k=0}^{K_h} \frac{\overline{p}_{r_{h,k}}(n)}{f_s^k k!} \ell^k \right) e^{-j2\pi \frac{f_h}{f_s}(n+\ell)} \right] - \tfrac{N-1}{2} \leq \ell \leq \tfrac{N-1}{2} \end{aligned} \tag{2}$$

where $p_{r_h}(t) = S_{r_h}(t)\, e^{j\left[\theta_{r_h}(t) - (r-1)\frac{2}{3}\pi\right]}$ is the dynamic synchrophasors of the $h-$th harmonic of phase $r = \{1,2,3\}$, $\overline{p}_{r_h}(t)$ is its complex conjugate counterpart, and $\left(p_{r_{h,k}}(n), \overline{p}_{r_{h,k}}(n)\right)$ is the pair of complex conjugate $k-$th order derivatives of the corresponding dynamic synchrophasors computed in the center of the data record, i.e., at time t_c.

If the samples of each phase of (2) are arranged into column vectors $\mathbf{s}_{r_n} = \left[s_r\left(\frac{n-N/2}{f_s}\right), \ldots s_r\left(\frac{n+N/2}{f_s}\right) \right]^T$, and the harmonics' Taylor's series coefficients are gathered into vector $\mathbf{p}_{r_n} = \left[p_{r_{1,0}}(n), \overline{p}_{r_{1,0}}(n), \ldots, p_{r_{H,K_H}}(n), \overline{p}_{r_{H,K_H}}(n) \right]^T$ for $r = \{1,2,3\}$, then expressions (2) can be more compactly rearranged in a matrix form as explained in [38], [39], i.e.,

$$\mathbf{s}_{r_n} = \mathbf{G}(\mathbf{f})\mathbf{p}_{r_n} \quad \text{for} \quad r = \{1,2,3\} \tag{3}$$

where the system matrix $\mathbf{G}(\cdot)$ includes orderly all the pairs of terms $\frac{\ell^k}{f_s^k k!} e^{j2\pi \frac{f_h}{f_s}(n+\ell)}$ and $\frac{\ell^k}{f_s^k k!} e^{-j2\pi \frac{f_h}{f_s}(n+\ell)}$ for $-\frac{N-1}{2} \leq \ell \leq \frac{N-1}{2}$ and $\mathbf{f} = [f_1, \ldots, f_H]^T$ is the vector including all harmonic frequencies. If the samples of a generic window function are collected into the diagonal matrix $\mathbf{W} = \text{diag}\left(w(\frac{-N+1}{2}, \ldots, w(\frac{N-1}{2})\right)$, so as to apply weighting to both sides of (3), then the estimation errors at the ends of each observation interval due to the truncation of the Taylor's series can be considerably reduced [34], [38]. Thus, the Taylor's series coefficients of the harmonic phasors can be computed by solving the resulting linear system based on (3), which yields

$$\begin{aligned} \widehat{\mathbf{p}}_{r_n} &= \left(\mathbf{G}^H(\mathbf{f})\mathbf{W}^H\mathbf{W}\mathbf{G}(\mathbf{f})\right)^{-1}\mathbf{G}^H(\mathbf{f}_0)\mathbf{W}^H\mathbf{W}\mathbf{s}_{r,n} = \\ &= \mathbf{F}_W(\mathbf{f})\mathbf{s}_{r,n} \quad \text{for} \quad r = \{1,2,3\} \end{aligned} \tag{4}$$

where ^{H} denotes the Hermitian operator, and $\mathbf{F}_W(\cdot)$ is the overall matrix of coefficients depending on the chosen window function. In this respect, the Kaiser window is used in the following, i.e.,

$$w(\ell) = \frac{I_0\left(\beta\sqrt{1 - \left(\frac{2\ell}{N-1} - 1\right)^2}\right)}{I_0(\beta)}, \; -\tfrac{N-1}{2} \leq \ell \leq \tfrac{N-1}{2} \tag{5}$$

where $I_0(\cdot)$ denotes the 0-order modified Bessel function of the first kind, while parameter β affects the shape of the window function and, consequently, the tradeoff between spectral main-lobe width and side-lobe levels.

Unfortunately, the application of (4) presents the following two main issues.

1) The computational complexity of the overall estimator for a given number of samples N tends to grow cubically with the total number $K_{tot} = \sum_{h=1}^{H} K_h$ of the Taylor's series coefficients of all harmonics included in the model. This is due to the fact that the size of matrix $\mathbf{G}^H(\mathbf{f})\mathbf{W}^H\mathbf{W}\mathbf{G}(\mathbf{f})$ in (4) is $2K_{tot} \times 2K_{tot}$ and the computational complexity of matrix inversion is of order $O(8K_{tot}^3)$.
2) The elements of $\mathbf{f}$ are just approximately known a priori, due to possible off-nominal frequency deviations.

Regarding the first issue, if $T = \frac{2}{f_0}$, then including $H = 4$ harmonics in the signal model is sufficient to achieve accurate estimates [37]. Moreover, while the fundamental components may exhibit significant fluctuations over time, the first- and second-order derivatives of the harmonics synchrophasors do not impact on estimation accuracy significantly and can be neglected. Therefore, in (2)-(4) we set $K_1 = 2$ and $K_2 = K_3 = K_4 = 0$.

The issue of the unknown frequency vector can instead be addressed by the 2-stage approach. In the first one, vector $\mathbf{f}_0 = [f_0, \ldots, H f_0]$ is used to compute matrix $\mathbf{F}_W(\cdot)$ in (4). Therefore, (4) can be rewritten as

$$\widehat{\mathbf{p}}_{r,n}^{(1)} = \mathbf{F}_W(\mathbf{f}_0)\mathbf{s}_{r,n} \quad \text{for} \quad r = \{1,2,3\} \tag{6}$$

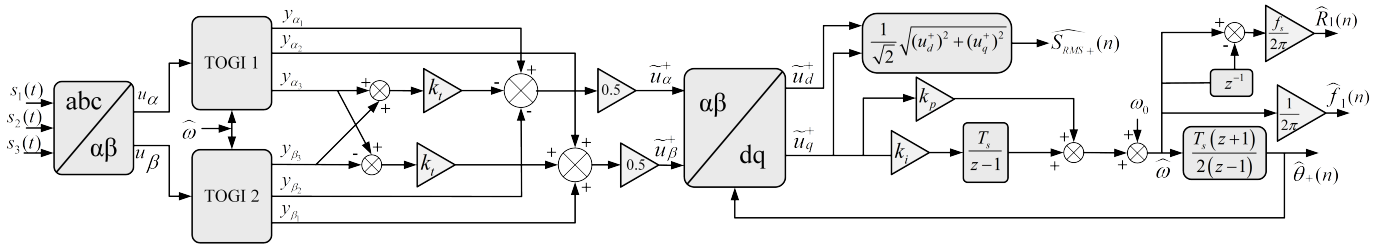

Fig. 2. Overall block diagram of the TOGI-PLL algorithm.

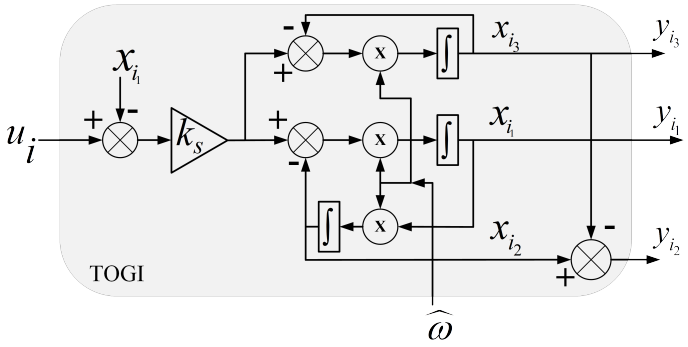

Fig. 3. Block diagram of the TOGI within the external PLL loop.

The zero- and first-order terms of the Taylor series of the fundamental synchrophasor extracted from $\widehat{\mathbf{p}}_n^{(1)}$ can then be used to estimate the frequencies of the $H = 4$ harmonics included in the model, i.e., [34]

$$\widehat{f}_{r_h}^{(1)} = h\left(f_0 + \frac{1}{2\pi}\frac{\mathrm{Im}\left\{\widehat{p}_{r_{1,1}}^{(1)}\widehat{\bar{p}}_{r_{1,0}}^{(1)}\right\}}{\left|\widehat{p}_{r_{1,0}}^{(1)}\right|^2}\right), \quad h = 1,\ldots,H \tag{7}$$

The frequency values returned by (7) and gathered into vector $\widehat{\mathbf{f}}_r^{(1)} = \left[\widehat{f}_{r_1}^{(1)},\ldots,\widehat{f}_{r_H}^{(1)}\right]^T$ can be used to update $\mathbf{F}_W(\cdot)$. Specifically, the second stage of the algorithm still relies on (4), but with a different matrix, i.e.,

$$\widehat{\mathbf{p}}_{r,n}^{(2)} = \mathbf{F}_W(\widehat{\mathbf{f}}_r^{(1)})\mathbf{s}_{r_n} \quad \text{for} \quad r = \{1,2,3\} \tag{8}$$

Quite importantly, while $\mathbf{F}_W(\mathbf{f}_0)$ can be precomputed and stored into memory once and for all, since its elements are constant, the matrix product returning $\mathbf{F}_W(\widehat{\mathbf{f}}_r^{(1)})$ must be recomputed every time the elements of $\widehat{\mathbf{f}}_r^{(1)}$ are updated. Therefore, despite the apparent similarity between (6) and (8), the second stage of the algorithm largely dominates the overall computational burden.

If the Fortescue transform is applied to the triple of fundamental synchrophasors returned by (8), then the estimated synchrophasors of the null, positive and negative sequence (denoted with subscripts 0, + and -, respectively) result from:

$$\begin{bmatrix}\widehat{p}_{0_{1,0}}\\ \widehat{p}_{+_{1,0}}\\ \widehat{p}_{-_{1,0}}\end{bmatrix} = \frac{1}{3}\begin{bmatrix}1 & 1 & 1\\ 1 & a & a^2\\ 1 & a^2 & a\end{bmatrix}\begin{bmatrix}\widehat{p}_{1_{1,0}}^{(2)}\\ \widehat{p}_{2_{1,0}}^{(2)}\\ \widehat{p}_{3_{1,0}}^{(2)}\end{bmatrix} \tag{9}$$

where $a = e^{j\frac{2\pi}{3}}$. Thus, the RMS value and the phase of the positive sequence component of (1) are given by:

$$\widehat{S}_{RMS_+}(n) = \sqrt{2}\left|\widehat{p}_{+_{1,0}}\right| \text{ and } \widehat{\theta}_+(n) = \arg\left\{\widehat{p}_{+_{1,0}}\right\} \tag{10}$$

Fundamental frequency and ROCOF can instead be estimated using the Taylor's series coefficients of all phases, since they can be reasonably assumed to be the same across the system. Therefore, if the expressions reported in [34] for frequency and ROCOF estimation are applied to each phase and the corresponding results are averaged, it follows that

$$\widehat{f}_1(n) = \frac{1}{3}\sum_{r=1}^{3}\left(\widehat{f}_{r_{1,0}}^{(1)} + \frac{1}{2\pi}\frac{\mathrm{Im}\left\{\widehat{p}_{r_{1,1}}^{(2)}\widehat{\bar{p}}_{r_{1,0}}^{(2)}\right\}}{\left|\widehat{p}_{r_{1,0}}^{(2)}\right|^2}\right) \tag{11}$$

$$\widehat{R}_1(n)=\frac{1}{3\pi}\sum_{r=1}^{3}\left(\frac{\mathrm{Im}\left\{\widehat{p}_{r_{1,2}}^{(2)}\widehat{\widehat{p}}_{r_{1,0}}^{(2)}\right\}}{2\left|\widehat{p}_{r_{1,0}}^{(2)}\right|^2}-\frac{\mathrm{Re}\left\{\widehat{p}_{r_{1,1}}^{(2)}\widehat{\widehat{p}}_{r_{1,0}}^{(2)}\right\}\mathrm{Im}\left\{\widehat{p}_{r_{1,1}}^{(2)}\widehat{\widehat{p}}_{r_{1,0}}^{(2)}\right\}}{\left|\widehat{p}_{r_{1,0}}^{(2)}\right|^4}\right) \tag{12}$$

While expressions (10)–(12) can be used to update the quantities of interest upon the arrival of each new waveform sample, frequency and ROCOF estimates may be averaged over one reporting interval before transmission to the PDC, thus reducing the impact of wideband noise.

B. Third-order generalized integrator PLL

Among the techniques for grid synchronization of PECs [22], the SRF PLLs are commonly adopted because they transform the three-phase signal from a stationary abc reference frame into a rotating dq frame that is aligned with the estimated grid voltage phasor [40]. This transformation simplifies the dynamic behavior analysis as well as the filtering requirements of the PLL, since the fundamental tone of the input voltage becomes a constant DC component in the rotating frame. A PI controller within the loop adjusts the estimated phase so that the quadrature component is driven to zero, thereby ensuring phase synchronization [40]. Unfortunately, standard SRF PLLs exhibit poor harmonic rejection and are sensitive to unbalanced conditions, which can introduce significant DC offsets. To improve phase-tracking performance and stability, more advanced PLL architectures are needed [41]. The use of Second-Order Generalized Integrators (SOGIs) after the PLL phase comparator improves harmonic attenuation in the rotating dq frame. Nevertheless, this enhancement alone is insufficient to meet PMU-grade accuracy. The TOGIs provide both better harmonic suppression and intrinsic open-loop DC-offset rejection [42]. Moreover, the TOGI-based PLL variant proposed in [24] achieves superior low-order harmonic cancellation, which motivates its adoption in this work.

Fig. 2 shows the overall block diagram of selected algorithm, that in the following will be referred to as TOGI-PLL. The three-phase input signal (1) is converted to orthogonal signals through the Clarke transformation, i.e.,

$$\begin{bmatrix}u_\alpha(t)\\u_\beta(t)\end{bmatrix}=\frac{2}{3}\begin{bmatrix}1 & -\frac{1}{2} & -\frac{1}{2}\\ 0 & \frac{\sqrt{3}}{2} & -\frac{\sqrt{3}}{2}\end{bmatrix}\begin{bmatrix}s_1(t)\\s_2(t)\\s_3(t)\end{bmatrix} \tag{13}$$

As shown in Fig. 2, $u_\alpha(t)$ and $u_\beta(t)$ are processed by two identical, TOGI filters running in parallel. Their structure is shown in Fig. 3 [43]. The state variables of either filter are denoted as $x_{\alpha_1}(t)$, $x_{\alpha_2}(t)$, $x_{\alpha_3}(t)$ and $x_{\beta_1}(t)$, $x_{\beta_2}(t)$, $x_{\beta_3}(t)$ for the α and β channels, respectively. Similarly, the corresponding output variables are $y_{\alpha_1}(t)$, $y_{\alpha_2}(t)$ and $y_{\alpha_3}(t)$, and $y_{\beta_1}(t)$, $y_{\beta_2}(t)$ and $y_{\beta_3}(t)$, respectively. Considering that the α and β TOGI stages are identical, their space-state equations are also the same, i.e.,

$$\begin{aligned}
\dot{x}_{i_1}(t)&=[k_s u_i t)-k_s x_{i_1}(t)-x_{i_2}(t)]\hat{\omega}(t)\\
\dot{x}_{i_2}(t)&=x_{i_1}(t)\hat{\omega}(t)\\
\dot{x}_{i_3}(t)&=[k_s u_i(t)-k_s x_{i_1}(t)-x_{i_3}(t)]\hat{\omega}(t)\ \text{ for } i=\{\alpha,\beta\}\\
y_{i_1}(t)&=x_{i_1}(t)\\
y_{i_2}(t)&=x_{i_2}(t)-x_{i_3}(t)\\
y_{i_2}(t)&=x_{i_3}(t)
\end{aligned} \tag{14}$$

where parameter $k_s=\sqrt{2}$, because this value provides the best tradeoff between filtering capability and transient duration [43], and $\hat{\omega}(t)$ is the feedback angular frequency estimated by the PLL.

It is worth emphasizing that in principle (14) is a nonlinear system as $\hat{\omega}(t)$ changes with time. However, under steady-state conditions, $\hat{\omega}(t)$ can be assumed approximately constant, i.e., $\hat{\omega}(t)\approx\hat{\omega}$. In this case, $\hat{\omega}$ can be regarded as a numerical coefficient of a linear dynamic system. Thus, from the Laplace transform of (14), after some algebraic steps, it results that the three transfer functions of the TOGI blocks are:

$$\begin{aligned}
D_{i_1}(s)&=\frac{Y_{i_1}(s)}{U_i(s)}=\frac{k_s\hat{\omega}s}{s^2+k_s\hat{\omega}s+\hat{\omega}^2}\\
D_{i_2}(s)&=\frac{Y_{i_2}(s)}{U_i(s)}=\frac{-k_s\hat{\omega}s(s-\hat{\omega})}{(s+\hat{\omega})(s^2+k_s\hat{\omega}s+\hat{\omega}^2)}\ \text{ for } i=\{\alpha,\beta\}\\
D_{i_3}(s)&=\frac{Y_{i_3}(s)}{U_i(s)}=\frac{k_s\hat{\omega}(s^2+\hat{\omega}^2)}{(s+\hat{\omega})(s^2+k_s\hat{\omega}s+\hat{\omega}^2)}
\end{aligned} \tag{15}$$

The frequency-domain analysis of (15) reveals that $D_{i_1}(s)$, $D_{i_2}(s)$ and $D_{i_3}(s)$ exhibit a band-pass behavior, unit gain with $\pi/2$ phase shift and a notch, respectively, at frequency $\hat{\omega}$ [24]. Thus, the output signals $y_{\alpha_1}(t)$, $y_{\alpha_2}(t)$ and $y_{\beta_1}(t)$, $y_{\beta_2}(t)$ can be used for Orthogonal Signal Generation (OSG), whereas signals $y_{\alpha_3}(t)$ and $y_{\beta_3}(t)$ (which do not contain the fundamental component) can be subtracted from the orthogonal components to mitigate possible disturbances, particularly low-order harmonics. If (1)

consists of just pure sine waves, then the orthogonal positive sequence components of (13) (denoted as $u_\alpha^+(t)$ and $u_\beta^+(t)$ in the following) can be extracted simply by cascading the Fortescue and the Clarke transformation. Thus, it results that [44]

$$\begin{aligned} u_\alpha^+(t) &= \frac{1}{2}\left(y_{\alpha_1}(t) - y_{\beta_2}(t)\right) \\ u_\beta^+(t) &= \frac{1}{2}\left(y_{\beta_1}(t) + y_{\alpha_2}(t)\right) \end{aligned} \tag{16}$$

Moreover, it is shown in [24] that, the harmonics affecting $u_\alpha^+(t)$ and $u_\beta^+(t)$ can be mitigated as follows, i.e.,

$$\begin{aligned} \tilde{u}_\alpha^+(t) &= u_\alpha^+(t) - \frac{k_t}{2}\left[y_{\alpha_3}(t) + y_{\beta_3}(t)\right] \\ \tilde{u}_\beta^+(t) &= u_\beta^+(t) + \frac{k_t}{2}\left[y_{\alpha_3}(t) - y_{\beta_3}(t)\right] \end{aligned} \tag{17}$$

where coefficient k_t affects the shape of transfer functions $\tilde{U}_\alpha^+(s)/U_\alpha(s)$ and $\tilde{U}_\beta^+(s)/U_\beta(s)$.

Although the preceding analysis is conducted in the continuous-time domain, in practice the input waveforms in (1) are sampled at a rate f_s, since the overall algorithm must run on a digital platform. To this end, the integrators depicted in Fig. (3) can be implemented with enhanced numerical accuracy by employing a third-order discrete-time integrator based on the following finite difference equation [45]:

$$o(n) = o(n-1) + \frac{1}{12f_s}[23d(n-1) - 16d(n-2) + 5d(n-3)] \tag{18}$$

where $d(\cdot)$ and $o(\cdot)$ denote the generic input and output sequences of one of such integrators. From the $z-$transform of (15), it results that the transfer functions of the discrete-time version of (14) can be obtained by replacing $s = \frac{12f_s(1-z^{-1})}{23z^{-1}-16z^{-2}+5z^{-3}}$ into (15).

The filtered orthogonal positive-sequence components in (17) are then transformed into a rotating dq frame using the Park transformation

$$\begin{bmatrix} u_d^+(n) \\ u_q^+(n) \end{bmatrix} = \begin{bmatrix} \cos\hat{\theta}(n) & \sin\hat{\theta}(n) \\ -\sin\hat{\theta}(n) & \cos\hat{\theta}(n) \end{bmatrix} \begin{bmatrix} \tilde{u}_\alpha^+(n) \\ \tilde{u}_\beta^+(n) \end{bmatrix} \tag{19}$$

The dq frame is synchronized with angle $\hat{\theta}(n)$, which is estimated by the PLL at time step $\frac{n}{f_s}$ and is fed back into the loop, as shown in Fig. 2. The RMS value of the positive sequence is proportional tothe sum in quadrature of the orthogonal dq components [46]

$$\widehat{S}_{RMS_+}(n) = \frac{1}{\sqrt{2}}\sqrt{(u_d^+(n))^2 + (u_q^+(n))^2} \tag{20}$$

while phase and frequency result from the innermost PLL loop in Fig. 2. Assuming that the PLL discrete-time Voltage Controlled Oscillator (VCO) is implemented with the trapezoidal method and that a Proportional and Integral (PI) controller with coefficients k_p and k_i and Euler integration is adopted, the innermost PLL loop dynamics in the rotating reference frame is described by the following space state model, i.e.,

$$\begin{aligned} u_i^+(n) &= u_i^+(n-1) + \frac{k_i}{f_s}u_q^+(n) \\ \hat{\omega}(n) &= \omega_0 + k_p u_q^+(n) + u_i^+(n) \\ \hat{\theta}(n) &= \hat{\theta}(n-1) + \frac{1}{2f_s}[\hat{\omega}(n) + \hat{\omega}(n-1)] \end{aligned} \tag{21}$$

where state variable $u_i^+(n)$ denotes the integral control action. Therefore, the synchrophasor angle and frequency of the orthogonal positive sequence at time step $\frac{n}{f_s}$ simply result from

$$\widehat{\theta}_+(n) = \hat{\theta}(n) \quad \text{and} \quad \widehat{f}_1(n) = \frac{\hat{\omega}(n)}{2\pi} \tag{22}$$

The ROCOF at the same time step instead can be computed from the first-order backward Euler difference equation, i.e. [46],

$$\widehat{R}_1(n) = \frac{f_s}{2\pi}[\hat{\omega}(n) - \hat{\omega}(n-1)], \tag{23}$$

Again, if the the system is used within a PMU, the frequency and ROCOF estimates returned by (22) and (23) may be averaged over one reporting interval to reduce the effect of possible disturbances (especially the wide-band noise) as explained at the end of Section II-A.

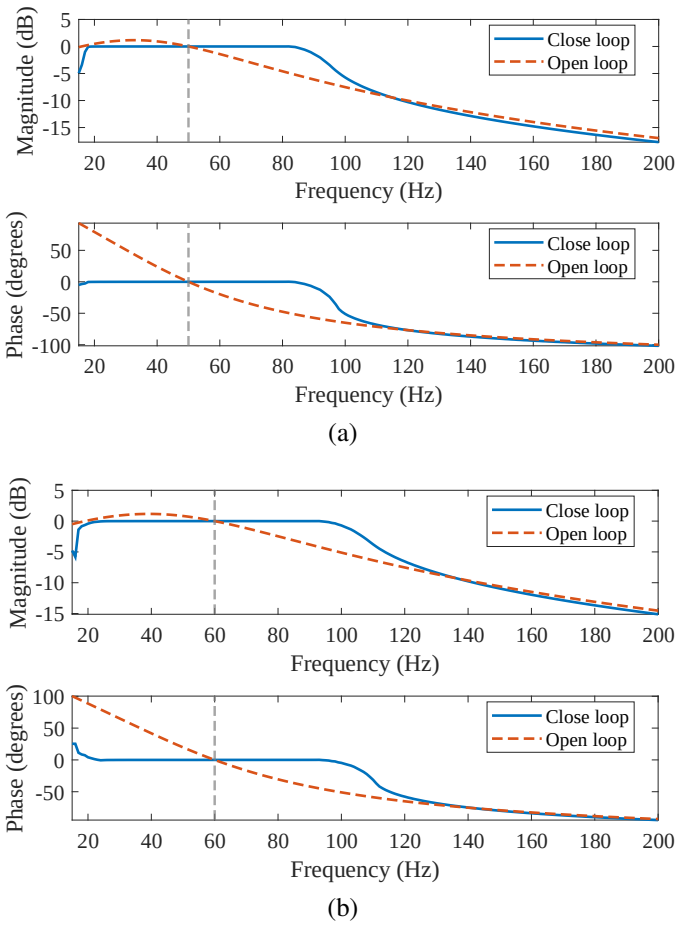

Fig. 4. Open-loop and closed-loop Bode diagrams of the TOGI-PLL for $f_0 = 50$ Hz (a) and $f_0 = 60$ Hz (b). In both cases, $k_t = \frac{1}{\sqrt{2}}$, $k_p = 20$ and $k_i = 100$.

III. Results and Performance Comparison

In this Section, the performance of the two algorithms under test described in Section II are first analyzed under the P Class testing conditions reported in the IEC/IEEE Standard 60255-118-1:2018 [31], and then considering the requirements for grid connection reported in the IEEE Standard 1547-2023 [30]. The nominal frequency f_0 is set to 50 Hz in the former kind of tests, and 60 Hz in the latter ones, both to differentiate the tests and to keep into account the fact that [30] is a US Standard. The sampling rate f_s is set to the minimal value avoiding aliasing when the signal contains 50th harmonics, i.e., $f_s = 6$ kHz. This choice keeps the computational burden as low as possible, resulting in only 120 or 100 samples per nominal cycle when $f_0 = 50$ Hz or 60 Hz, respectively. It is important to highlight that while for PMU-based monitoring applications, the output values can be decimated (and therefore averaged in the case of frequency and ROCOF measurements) over every reporting period, for grid synchronization the sample-by-sample results shall be reported.

As far as the algorithms' settings are concerned, it is worth reminding that:

- In the 2-stage TLTFT algorithm case, $N = \{239, 199\}$ samples at a time are processed when $f_0 = 50$ Hz or 60 Hz, respectively. Also, a Kaiser window with $\beta = 4$ is used, as this value provides the best tradeoff between synchrophasor, frequency and ROCOF estimation accuracy. In fact, setting $\beta > 4$ just increases the sensitivity to wideband noise with no significant benefits in terms of harmonics rejection or synchrophasor tracking capability [29].
- In the TOGI-PLL algorithm, parameter k_t is set to $\frac{1}{\sqrt{2}}$, as this value provides a good out-of-band attenuation while ensuring that the filter gain at frequency $\hat{\omega}$ is equal to 1 [24]. Moreover, the PI controller coefficients k_p and k_i are set to 20 and 100, respectively. These values were determined through numerical simulations by exploring the neighborhood of the parameters reported in [24], and selecting the configuration that yields the shortest settling time of the TOGI-PLL.

The open-loop and closed-loop Bode diagrams of the TOGI-PLL are shown in Fig. 4(a)-(b), for $f_0 = 50$ Hz and $f_0 = 60$ Hz, respectively. Due to the PLL inherent nonlinear nature, both frequency responses were estimated using the so-called perturbation method [47], i.e., by stimulating the PLL with a three-phase signal of amplitude equal 1 p.u. and increasing the frequency from 1 Hz to 100 Hz in steps of 1 Hz. The Bode diagrams confirm the band-pass behavior of the PLL (namely the expected

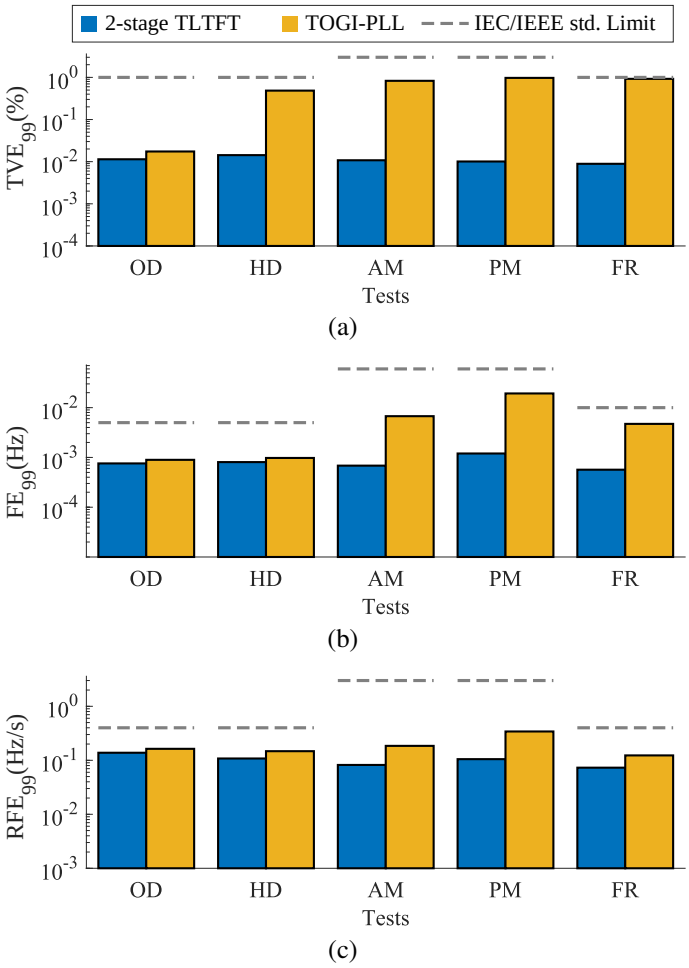

Fig. 5. 99th percentiles of the (a) TVE, (b) FE and (c) RFE values in different P Class testing conditions reported in the IEC/IEEE Standard 60255-118-1:2018 when either the 2-stage TLTFT (with $\beta = 4$ in the Kaiser window) or the TOGI-PLL (with $k_p = 20$ and $k_i = 100$) are used. The dashed lines represent the IEC/IEEE Standard limits in different testing conditions.

capability to attenuate DC offsets and harmonics) as well as the flat closed-loop amplitude and the phase responses (with unit gain and zero phase shift) around the chosen nominal frequency f_0.

A. PMU compliance tests

The P Class testing conditions reported in the IEC/IEEE Standard 60255-118-1:2018 and considered in the rest of this Section are briefly summarized below [31].

- **Off-nominal Deviation (OD)**: the RMS value of the fundamental component is increased from 0.8 p.u. to 1.2 p.u. at 0.1 p.u. steps and the system frequency changes by ± 2 Hz with 0.1 Hz steps.
- **Harmonic Distortion (HD)**: all harmonics from the 2nd to the 50th are added (one at a time) to the fundamental tone. The RMS value of each added harmonic is 1% of the fundamental.
- **Amplitude Modulation (AM)**: the voltage amplitude is affected by 10% sinusoidal amplitude modulation with a modulating frequency of 2 Hz.
- **Phase Modulation (PM)**: the voltage amplitude is affected by a sinusoidal phase modulating tone of amplitude 0.1 rad and frequency 2 Hz.
- **Frequency Ramp (FR)**: the signal frequency is increased or decreased linearly by no more than ± 2 Hz with respect to the fundamental frequency at a rate of ± 1 Hz/s.

In all tests, the acquired waveforms are affected by additive wideband noise. Although the presence of noise is not explicitly considered in [31], its inclusion in the simulations increases the realism of the results, as it accounts for the noise introduced by the signal acquisition front-end of high-resolution measurement devices. Thus, the Signal-to-Noise Ratio (SNR) is set to 70 dB. Fig. 5(a)-(c) depicts the bar diagrams representing the 99th percentiles of Total Vector Errors (TVE), Frequency Estimation Errors (FE) and ROCOF Estimation Errors (RFE), respectively, obtained with both algorithms under test. The data records are shifted by one sample at a time and output values are decimated, assuming a reporting rate of 50 frame/s. Each test is

performed on 2-second-long waveforms, after the completion of the initial transient. The dashed lines in Fig. 5(a)-(c) represent the P Class limits specified in the IEC/IEEE Standard in the various testing conditions listed above.

The bar diagram confirm that the P Class limits are met in all cases, with the 2-stage TLTFT algorithm that generally outperforms the TOGI-PLL. In the FR test, the TVE values obtained with the TOGI-PLL reach the IEC/IEEE Standard limit due to the large phase errors occurring during the transients at the beginning and at the end of the frequency ramp. Interestingly, simulations indicate that including the 2nd, 3rd, and 4th harmonic phasors in the parameter vector of the 2-stage TLTFT algorithm offers more effective harmonic mitigation than the cancellation technique employed by the TOGI-PLL. In fact, the maximum TVE, FE and RFE values obtained with the 2-stage TLTFT algorithm under the effect of harmonics are comparable with those obtained in the OD test case. Surprisingly, the TOGI-PLL is quite more sensitive to amplitude and, above all, phase oscillations (see AM and PM results) than the 2-stage TLTFT algorithm.

Figs. 6 and 7 show the TVE (a), absolute FE (b) and absolute RFE (c) profiles in the transient conditions specified in the IEC/IEEE Standard, namely after a 10% magnitude step or a 10° phase step, respectively [31]. The response times defined by the IEC/IEEE Standard are measured from the instant when the TVE, $|\mathrm{FE}|$ and $|\mathrm{RFE}|$ curves first exceed the specified thresholds (indicated by dashed lines in each plot) to the instant after which they remain below those thresholds.

The results of step tests reveal an excellent responsiveness of the 2-stage TLTFT algorithm, that is superior to the TOGI-PLL in this regard as well. The TVE of the 2-stage TLTFT algorithm falls below the 1% threshold within approximately half a cycle in amplitude step tests and within about one cycle in phase step tests. In comparison, the corresponding synchrophasor response times of the TOGI-PLL are approximately 1.1 and 1.8 cycles, respectively. In any case, such values are below the 2-cycle IEC/IEEE Standard limit for P Class PMUs.

The performance gap becomes instead quite larger when the frequency and ROCOF response times are considered. Specifically, the 2-stage TLTFT algorithm consistently achieves response times of approximately two cycles (well below the IEC/IEEE Standard limits, which are 4.5 cycles for frequency and 6 cycles for ROCOF, respectively). In contrast, the TOGI-PLL exhibits response times ranging from 4.4 to 6.2 cycles, occasionally exceeding the Standard's thresholds. Moreover, the peak values of TVE, $|\mathrm{FE}|$, and $|\mathrm{RFE}|$ observed during transients with the TOGI-PLL are approximately 2 to 20 times higher than those recorded with the 2-stage TLTFT algorithm.

B. DER connection/disconnection compliance tests

In this Section, the performance of the two algorithms described in Section II is evaluated against selected grid code requirements outlined in the IEEE Standard 1547-2018 for DER connection and disconnection [30]. Specifically, Table I reports:

1) the maximum allowable RMS amplitude, frequency, and phase differences between voltage waveforms at the interface between the EPS and a DER for different DER rated power levels;
2) the expanded uncertainty values (with a 99% confidence level) associated with the sample-by-sample measurements of RMS amplitude, frequency, and phase performed with both algorithms at the end of the transient for connecting a DER to the EPS under either balanced and unbalanced conditions. The unbalanced case assumed a ratio negative/positive sequence component amplitudes (i.e., a Voltage Unbalance Factor – VUF), equal to 2%, which is in accordance with the values adopted in other studies (e.g., [48]) and it is also consistent with the limits specified in the EN Standard 50160:2022 for European distribution systems [49].

The expanded uncertainty values were obtained through Monte Carlo simulations conducted under borderline, yet realistic operating conditions. Specifically, we simulated the connection of a DER to a Medium Voltage (MV) EPS affected by static frequency deviations within ± 3 Hz, with a Total Harmonic Distortion (THD) equal to 5% arising from the superimposition of the first 25 harmonics of amplitude approximately equal to 1.5% of the fundamental, on average. Such operating conditions are compliant with the MV requirements reported in both the EN Standard 50160:2022 [49]. and the IEEE Standard 519-2022 [50], dealing with harmonics control in electric power systems.

Compared with the tests reported in Section III-A, the wide-band noise floor was purposely increased to reach a Signal-to-Noise Ratio (SNR) of 55 dB at the point of DER connection. Such larger noise level is intended to model the influence of measurement transducers and other electrical equipment present in the system. For each off-nominal frequency deviation, 120 simulation runs were performed. Observe that in all considered cases the impact of a possible unbalance is almost negligible, as both algorithms tend to estimate the RMS value, the phase and the frequency of the extracted positive sequence component only. However, the expanded uncertainty values associated with the 2-stage TLTFT algorithms are significantly lower than the TOGI-PLL ones. In particular, while the 2-stage TLTFT algorithm accuracy in measuring voltage magnitude, frequency and phase at the point of DER connection is at least one order of magnitude below the most stringent limits shown in the central columns of Table I, the TOGI-PLL fails to meet the frequency accuracy requirements when DERs with a large rated-power are considered.

Nonetheless, it should not be forgotten that the reported uncertainty values refer to sample-by-sample estimates. In fact, simulations show that frequency and ROCOF uncertainties could be reduced by more than one order of magnitude by averaging the results over one or more cycles. This is explicitly acknowledged by the IEEE Standard 1547-2018 as well. Indeed, the

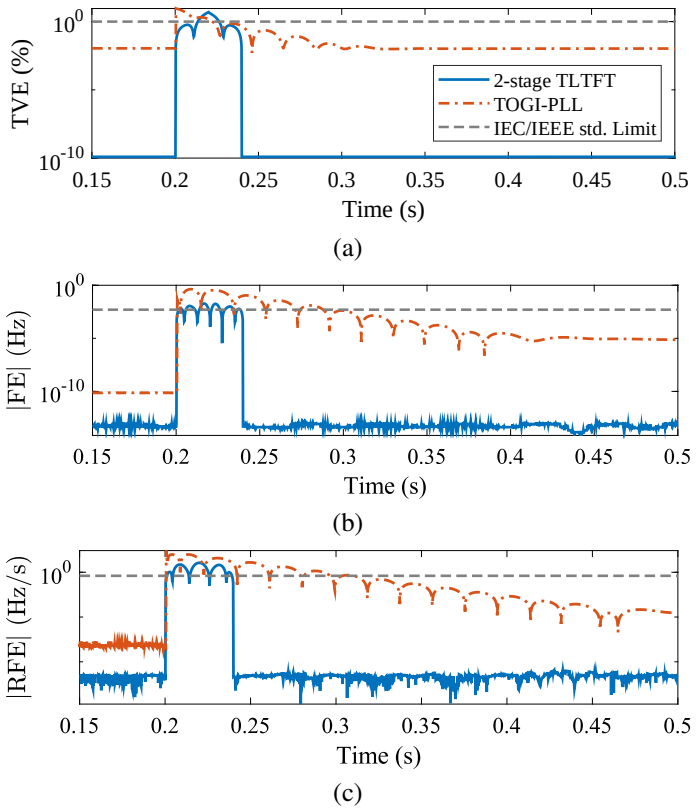

Fig. 6. TVE (a), absolute FE (b) and absolute RFE (c) values obtained with the 2-stage TLTFT and the TOGI-PLL after a 10% positive amplitude step is applied. The dashed lines refer to the IEC/IEEE Standard 60255-118-1:2018 thresholds that are used for response time computation.

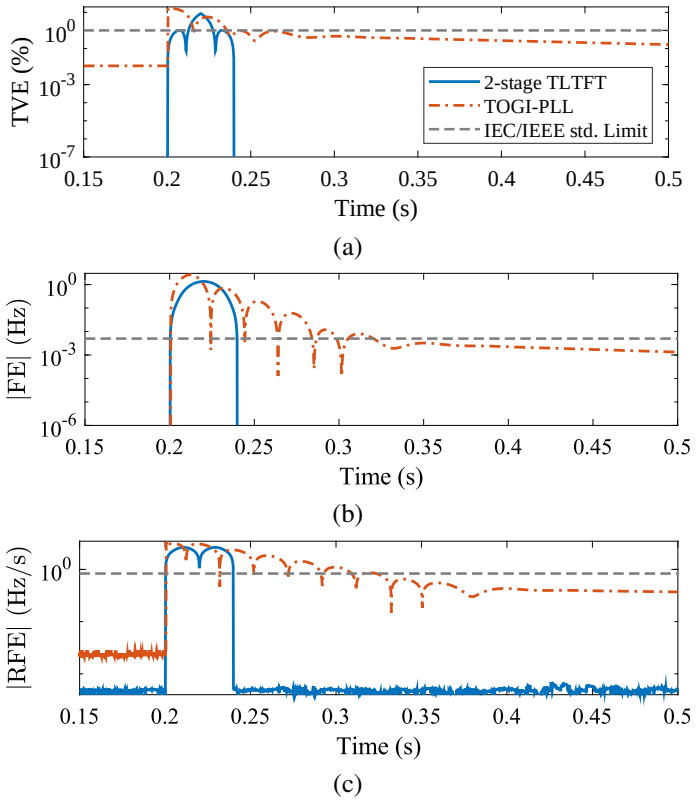

Fig. 7. TVE (a), absolute FE (b) and absolute RFE (c) values obtained with the 2-stage TLTFT and the TOGI-PLL after a 10° positive phase step is applied. The dashed lines refer to the IEC/IEEE Standard 60255-118-1:2018 thresholds that are used for response time computation.

TABLE I

COMPARISON BETWEEN THE MAXIMUM VOLTAGE MAGNITUDE, PHASE, AND FREQUENCY DIFFERENCES SPECIFIED IN THE IEEE STD. 1547-2018 FOR DER CONNECTION, AND THE MEASUREMENT ACCURACY ACHIEVED BY THE 2-STAGE TLTFT ALGORITHM AND THE TOGI-PLL UNDER BALANCED OR UNBALANCED CONDITIONS. IN BOTH CASES, THE FUNDAMENTAL FREQUENCY IS CHANGED BY ± 3 HZ, THD = 5% AND SNR = 55 DB.

	IEEE Std. 1547-2018 limits for DER-EPS interconnection			$\mathbf{U_{99}}$			
				Balanced		**Unbalanced (VUF=2%)**	
	$\mathbf{P \leq 500}$ **kVA**	$\mathbf{500 < P \leq 1500}$ **kVA**	$\mathbf{P > 1500}$ **kVA**	**2-stage TLTFT**	**TOGI-PLL**	**2-stage TLTFT**	**TOGI-PLL**
$\mathbf{\Delta V}$ **(%)**	10	5	3	**0.07**	**0.75**	**0.07**	**0.92**
$\mathbf{\Delta f}$ **(mHz)**	300	200	100	**11.2**	**157**	**11.5**	**159**
$\mathbf{\Delta \Phi}$ **(°)**	20	15	10	**0.04**	**0.23**	**0.04**	**0.23**

TABLE II

COMPARISON BETWEEN THE CLEARING TIME REQUIREMENTS OF THE IEEE STD. 1547-2018 UNDER ABNORMAL MAGNITUDE AND FREQUENCY STEP CHANGES CAUSING DER TRIPPING, AND THE MAXIMUM SETTLING TIME OF 2-STAGE TLTFT AND TOGI-PLL.

Step test condition	**Variation**	**IEEE Std. 1547-2018 clearing time (s)**	**Max. meas. settling time (s)**	
			2-stage TLTFT	**TOGI-PLL**
Over-voltage	$+20\%$	0.16	0.001	0.013
Under-voltage	-50%	2.0	0.017	0.017
Over-frequency	$+2$ Hz	0.16	0.022	0.074
Under-frequency	-3 Hz	0.16	0.021	0.215

voltage magnitude and frequency measurement accuracy requirements specified in Table 3 of [30] (i.e., $\pm 1\%$ and ± 10 mHz in steady state and $\pm 2\%$ and ± 100 mHz during transients, respectively) refer to measurement windows of 10 cycles in stationary conditions (60 cycles for frequency) and 5 cycles during transients.

Therefore, both the considered algorithms could be used to synchronize the interconnection of a DER to the EPS. While the overall settling time following DER connection depends also, and above all, on the control loop within the PEC, the settling times of both grid synchronization algorithms (consisting of few cycles based on the results shown in Section III-A) are orders of magnitude lower than the typical enter into service time intervals specified in [30] (that are indeed in the order of seconds).

Further Monte Carlo simulations were performed to test the ability of the two algorithms under test to promptly detect the most severe abnormal conditions leading to DER tripping according to the IEEE Standard 1547-2018 [30]. Specifically, four complementary testing conditions are considered:

- a sudden voltage amplitude increase by 20%;
- a sudden voltage amplitude drop by 50%;
- a sudden voltage frequency increase by 2 Hz;
- a sudden voltage frequency decrease by -3 Hz.

In all the testing conditions listed above, the SNR is set again to 55 dB, while the THD is lower than in the previous DER connection scenario (i.e., 2.5% with individual voltage harmonics of amplitude smaller than 1.5% of the fundamental, as indicated in Table 3 of [30]). Table II reports the maximum latencies of each algorithm in reaching convergence, i.e., within $\pm 2\%$ of the final RMS value for amplitude step changes and within ± 100 mHz of the final frequency value for frequency step changes. Such convergence thresholds coincide with the measurement accuracy limits during transients indicated in Table 3 of [30], with the raw measurement data averaged over one cycle (instead of 5 cycles) as the one-cycle average is sufficient to achieve the wanted accuracy in all cases. The maximum latency values are computed by changing randomly the time when the step occurs within a given cycle. The results in Table II demonstrate that the measurement settling times of the 2-stage TLTFT algorithm are at last one order of magnitude shorter than the maximum clearing times specified in [30], whereas the TOGI-PLL exhibits controversial results. On the one hand, it is very rapid to support the required clearing operations in the case of sudden amplitude changes. On the other hand, it may exhibit excessively long transients, potentially exceeding compliance limits, when large frequency steps occur.

C. Execution Times

Both algorithms were implemented in MATLAB R2018b and were tested on a laptop equipped with 16 GB RAM and an Intel Core i7-11370H processor running at 3.30 GHz. The execution times, considering the settings described at the beginning of Section III are:

- for **2-state TLTFT**: 3 ms on average (4.7 ms max);
- for **TOGI-PLL**: 18 μs on average (20 μs max).

This significant performance gap is due to the fact that in the 2-stage TLTFT algorithm the complexity of matrix product operations in (8) is of order $O(2K_{tot}N^2)$, where $N >> 2K_{tot}$, e.g., $N \approx 240$ or ≈ 200 samples for $f_0 = 50$ Hz or 60 Hz,

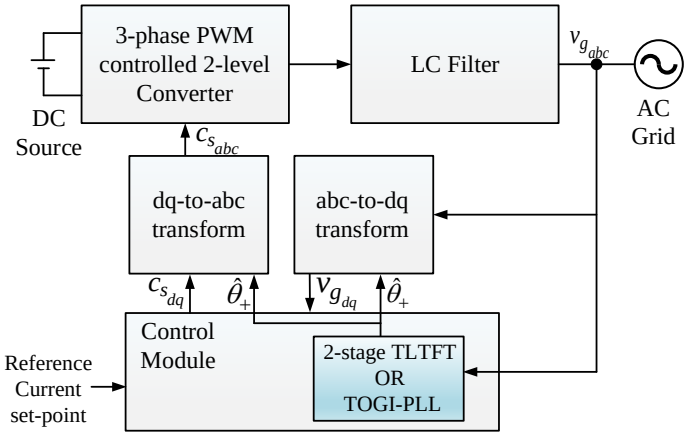

Fig. 8. Simplified block diagram of the PEC described in [51]. The 2-stage TLTFT algorithm and the TOGI-PLL algorithm are alternatively used for grid synchronization, replacing the native SRF PLL.

respectively. In contrast, the TOGI-PLL operates only on a few samples per iteration, yielding outputs with a much lower computational burden.

Both algorithms meet the real-time reporting rate requirements specified in the IEC/IEEE Standard 60255-118-1:2018. However, the 2-stage TLTFT algorithm requires further optimization to improve real-time performance. In particular, since reducing the sampling rate is not feasible and matrix $\mathbf{F}_W(\mathbf{f}_0)$ is already precomputed, additional improvements in computational efficiency could be achieved by:

- expressing the Taylor series coefficients and the system matrices in rectangular coordinates to allow separate processing of real and imaginary parts, as suggested in [37];
- implementing the entire algorithm in low-level programming languages such as C or C++, which could yield a speed-up factor of nearly one order of magnitude, when the algorithm runs on the same hardware;
- better exploiting the parallel computing capabilities of the available processing platforms (if any).

IV. Validation through PEC-level simulations

The simulation results reported in Sections III-A and III-B are essential for performance evaluation, but they are not sufficient to verify the correct operation of a PEC. Indeed, both the 2-stage TLTFT algorithm and the TOGI-PLL may interact with the internal PEC dynamics, potentially affecting its performance, stability, or both. Although a detailed stability analysis depends on the specific PEC architecture and, consequently, it is beyond the scope of this work, showing an example of PEC closed-loop behavior is crucial to assess the feasibility of the general idea developed in this study. To this end, the native SRF PLL of the PEC described in [51] was replaced with either the 2-stage TLTFT algorithm or the TOGI-PLL. A simplified block diagram of the overall PEC is shown in Fig. 8. The setup consists of a two-level voltage-source converter (VSC) controlled by a pulse-width modulator (PWM), supplied by a constant DC input voltage. The VSC generates a three-phase waveform in the abc coordinate frame, while the control module operates in the dq frame. The selected grid synchronization algorithm tracks the phase of AC grid voltage signal and returns the estimated phase angle $\hat{\theta}_+$, that is computed from (10) or (22) depending on whether the 2-stage TLTFT or the TOGI-PLL is used, respectively. The estimated angle is then used by the control module (which is designed to follow a given reference current) to generate the reference phase angles for the dq-to-abc and abc-to-dq frame transformations. In particular, the control signal $c_{s\,dq}$ based on $\hat{\theta}_+$ is transformed into the abc frame to drive the PWM modulator. The simulations of the overall PEC model are performed in Matlab/Simulink with a fixed time step of 1 μs, but assuming that the input and output signals of the digital control module are sampled at $f_s = 10$ kHz. This value is higher than the sampling frequency used in the tests described in Section III. In this case study, $f_0 = 50$ Hz and the THD of the AC grid voltage is the same as in the last example described in Section III-B, i.e., 2.5% with the individual harmonics being smaller than 1.5% of the fundamental. The settings of the 2-stage TLTFT algorithm and the TOGI-PLL are the same as those described in Section III, except for N and the TLTFT buffer size that now consists of 399 locations to account for the higher sampling rate. The simulation results obtained with either algorithm are shown in Fig. 9(a)-(b). Fig. 9(a) displays the estimated RMS value, the frequency, and the phase angle of the grid voltage positive sequence component, whereas Fig. 9(b) shows the three-phase output voltage signals generated by the PEC. After the initial transients, both algorithms accurately estimate the grid voltage parameters and maintain phase locking between the converter and the grid without noticeable stability issues. Although PLLs can, under certain conditions, trigger nearly synchronous sideband oscillations near the fundamental frequency [52], neither the 2-stage TLTFT nor the TOGI-PLL introduce resonance peaks that could lead to harmonic instability. Therefore, under the considered conditions, both algorithms demonstrate stable and reliable performance for PEC grid-synchronization purposes.

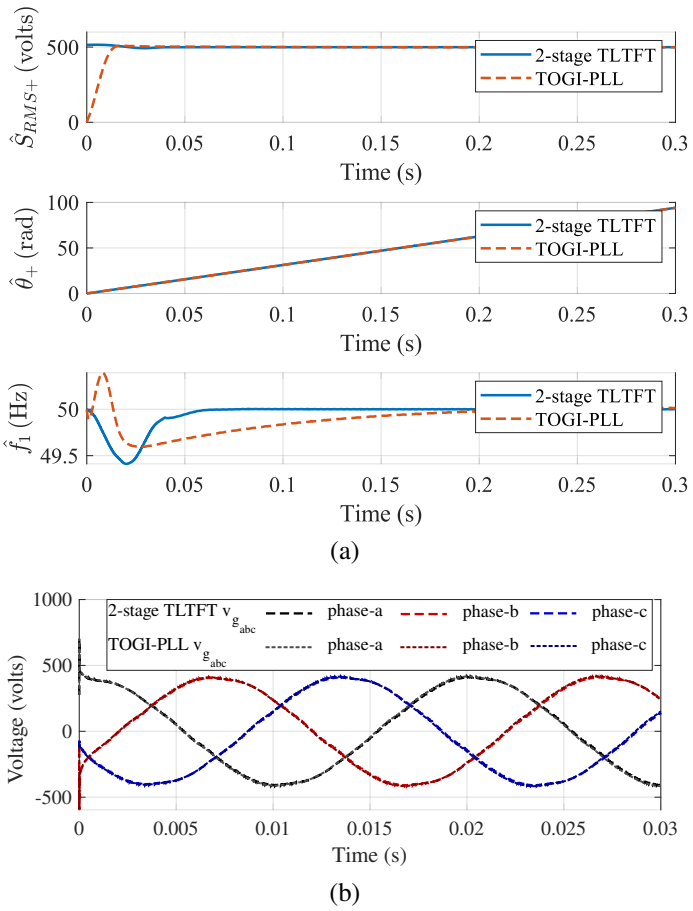

Fig. 9. (a) RMS amplitude, phase and frequency estimated by the 2-stage TLTFT or the TOGI-PLL when either algorithm is placed into the control loop of the PEC described in [51] for grid synchronization; (b) three-phase waveforms generated by the PEC in either case.

V. Conclusions

The adoption of a common algorithm for both grid synchronization and monitoring to be integrated in the control unit of a smart power electronic converter can enhance distribution system observability at limited additional cost, while enabling flexible interconnection of distributed energy resources (DERs). This study explores the feasibility of this idea by comparing two algorithms, originally designed for one function and adapted to the other.

The 2-stage TLTFT algorithm, derived from PMU applications, meets the IEC/IEEE 60255-118-1:2018 (P Class) and IEEE 1547-2018 requirements. Although simpler than other TFT-based solutions, it is still much slower than the TOGI-PLL, and requires further optimizations. In contrast, the TOGI-PLL (originally conceived for grid synchronization, but with higher harmonic rejection and DC offset cancellation capability) achieves very short execution times and P Class compliance. However, its transient response under abrupt phase or frequency changes is limited. Despite the respective limitations of either algorithm and their quite different delays, both of them were successfully used for grid synchronization of a converter model with no evident stability problems.

Future work will be focused on the computational burden reduction of the 2-stage TLTFT algorithm and on the improvement of the TOGI-PLL performance under dynamic conditions.

Acknowledgment

The Authors would like to thank Dr. Federico Cecati from the University of Trento, for his important support and advise in addressing some of the Reviewers' remarks on this work.

References

[1] G. Barchi, M. G. Prina, and D. Moser, "A PV hosting capacity assessment in distribution grids: towards the 2030 and 2050 energy scenarios," in *2023 AEIT International Annual Conference (AEIT)*, 2023, pp. 1–6.

[2] M. Secchi, G. Barchi, D. Macii, and D. Petri, "Smart electric vehicles charging with centralised vehicle-to-grid capability for net-load variance minimisation under increasing EV and PV penetration levels," *Sustainable Energy, Grids and Networks*, vol. 35, p. 101120, 2023.

[3] G. Barone, A. Buonomano, C. Forzano, A. Palombo, and G. Russo, "The role of energy communities in electricity grid balancing: A flexible tool for smart grid power distribution optimization," *Renewable and Sustainable Energy Reviews*, vol. 187, p. 113742, 2023.

[4] M. Secchi, G. Barchi, D. Macii, D. Moser, and D. Petri, "Multi-objective battery sizing optimisation for renewable energy communities with distribution-level constraints: A prosumer-driven perspective," *Applied Energy*, vol. 297, p. 117171, 2021.

[5] E. B. Alzate, M. Bueno-López, J. Xie, and K. Strunz, "Distribution system state estimation to support coordinated voltage-control strategies by using smart meters," *IEEE Transactions on Power Systems*, vol. 34, no. 6, pp. 5198–5207, 2019.

[6] A. Bashian, D. Macii, D. Fontanelli, and D. Petri, "A Tuned Whitening-Based Taylor-Kalman Filter for P Class Phasor Measurement Units," *IEEE Transactions on Instrumentation and Measurement*, vol. 71, pp. 1–13, 2022.

[7] S. Bu, L. G. Meegahapola, D. P. Wadduwage, and A. M. Foley, "Stability and dynamics of active distribution networks (ADNs) with D-PMU technology: A review," *IEEE Transactions on Power Systems*, vol. 38, no. 3, pp. 2791–2804, 2023.

[8] C. Muscas, M. Pau, P. A. Pegoraro, and S. Sulis, "Effects of measurements and pseudomeasurements correlation in distribution system state estimation," *IEEE Transactions on Instrumentation and Measurement*, vol. 63, no. 12, pp. 2813–2823, 2014.

[9] D. Della Giustina, M. Pau, P. A. Pegoraro, F. Ponci, and S. Sulis, "Electrical distribution system state estimation: measurement issues and challenges," *IEEE Instrumentation & Measurement Magazine*, vol. 17, no. 6, pp. 36–42, 2014.

[10] N. M. Manousakis, G. N. Korres, and P. S. Georgilakis, "Taxonomy of PMU placement methodologies," *IEEE Transactions on Power Systems*, vol. 27, no. 2, pp. 1070–1077, 2012.

[11] P. A. Pegoraro, A. Meloni, L. Atzori, P. Castello, and S. Sulis, "PMU-based distribution system state estimation with adaptive accuracy exploiting local decision metrics and IoT paradigm," *IEEE Transactions on Instrumentation and Measurement*, vol. 66, no. 4, pp. 704–714, 2017.

[12] S. Kumar, B. Tyagi, V. Kumar, and S. Chohan, "Optimization of phasor measurement units placement under contingency using reliability of network components," *IEEE Transactions on Instrumentation and Measurement*, vol. 69, no. 12, pp. 9893–9906, 2020.

[13] R. Andreoni, D. Macii, M. Brunelli, and D. Petri, "Tri-objective optimal PMU placement including accurate state estimation: The case of distribution systems," *IEEE Access*, vol. 9, pp. 62 102–62 117, 2021.

[14] A. Alimardani, F. Therrien, D. Atanackovic, J. Jatskevich, and E. Vaahedi, "Distribution system state estimation based on nonsynchronized smart meters," *IEEE Transactions on Smart Grid*, vol. 6, no. 6, pp. 2919–2928, 2015.

[15] M. Pau, E. Patti, L. Barbierato, A. Estebsari, E. Pons, F. Ponci, and A. Monti, "Design and accuracy analysis of multilevel state estimation based on smart metering infrastructure," *IEEE Transactions on Instrumentation and Measurement*, vol. 68, no. 11, pp. 4300–4312, 2019.

[16] M. R. Ahmed, J. M. Cano, P. Arboleya, L. S. Ramón, and A. Y. Abdelaziz, "DSSE in European-Type Networks Using PLC-Based Advanced Metering Infrastructure," *IEEE Transactions on Power Systems*, vol. 37, no. 5, pp. 3875–3888, 2022.

[17] G. Barchi and D. Macii, "Robust Distribution System State Estimation Based on Smart Meter Data Under High PV Penetration," in *2024 International Conference on Smart Energy Systems and Technologies (SEST)*, 2024, pp. 1–6.

[18] S. Song, H. Xiong, Y. Lin, M. Huang, Z. Wei, and Z. Fang, "Robust three-phase state estimation for PV-integrated unbalanced distribution systems," *Applied Energy*, vol. 322, p. 119427, 2022.

[19] G. Barchi and D. Macii, "A photovoltaics-aided interlaced extended Kalman filter for distribution systems state estimation," *Sustainable Energy, Grids and Networks*, vol. 26, p. 100438, 2021.

[20] European Commission, "Commission Regulation (EU) 2016/631 of 14 April 2016 establishing a network code on requirements for grid connection of generators," Official Journal of the European Union, L 112/1, Apr. 2016, available at: https://eur-lex.europa.eu/legal-content/EN/TXT/?uri=CELEX:32016R0631.

[21] Xu, Shuang and Xue, Yaosuo and Chang, Liuchen, "Review of power system support functions for inverter-based distributed energy resources- standards, control algorithms, and trends," *IEEE Open Journal of Power Electronics*, vol. 2, pp. 88–105, 2021.

[22] F. D. Freijedo, J. Doval-Gandoy, O. Lopez, C. Martinez-Peñalver, A. G. Yepes, P. Fernandez-Comesaña, J. Malvar, A. Nogueiras, J. Marcos, and A. Lago, "Grid-synchronization methods for power converters," in *2009 35th Annual Conference of IEEE Industrial Electronics*, 2009, pp. 522–529.

[23] F. Messina, P. Marchi, L. Rey Vega, C. G. Galarza, and H. Laiz, "A Novel Modular Positive-Sequence Synchrophasor Estimation Algorithm for PMUs," *IEEE Transactions on Instrumentation and Measurement*, vol. 66, no. 6, pp. 1164–1175, 2017.

[24] V. N. Giotopoulos and G. N. Korres, "A Laboratory PMU Based on Third-Order Generalized Integrator Phase-Locked Loop," *IEEE Transactions on Instrumentation and Measurement*, vol. 73, pp. 1–11, 2024.

[25] D. Fontanelli and D. Macii, "Accurate time synchronization in PTP-based industrial networks with long linear paths," in *ISPCS 2010 - 2010 International IEEE Symposium on Precision Clock Synchronization for Measurement, Control and Communication, Proceedings*, 2010, p. 97 – 102.

[26] IEEE Std. C37.238-2017, "IEEE standard profile for use of IEEE 1588 precision time protocol in power system applications," pp. 1–42, 2017.

[27] J. Benzaquen, M. Miranbeigi, P. Kandula, and D. Divan, "Collaborative autonomous grid-connected inverters: Flexible grid-forming inverter control for the future grid," *IEEE Electrification Magazine*, vol. 10, no. 1, pp. 22–29, 2022.

[28] R. Nicolosi, L. Piegari, and A. Benigni, "A smart PV inverter controller with PMU capability," in *2016 Clemson University Power Systems Conference (PSC)*, 2016, pp. 1–7.

[29] A. Singh, D. Macii, and D. Petri, "Embedding PMU algorithms in grid-following converters: a feasibility study," in *2025 IEEE Instrumentation and Measurement Technology Conference (I2MTC)*, 2025.

[30] IEEE Std 1547-2018 (Revision of IEEE Std 1547-2003), "IEEE standard for interconnection and interoperability of distributed energy resources with associated electric power systems interfaces," pp. 1–138, 2023.

[31] IEC/IEEE 60255-118-1:2018, "IEEE/IEC international standard - measuring relays and protection equipment - part 118-1: Synchrophasor for power systems - measurements," pp. 1–78, 2018.

[32] P. Castello, R. Ferrero, P. A. Pegoraro, and S. Toscani, "Space Vector Taylor–Fourier Models for Synchrophasor, Frequency, and ROCOF Measurements in Three-phase Systems," *IEEE Transactions on Instrumentation and Measurement*, vol. 68, no. 5, pp. 1313–1321, 2019.

[33] J. A. de la O Serna, "Dynamic phasor estimates for power system oscillations," *IEEE Transactions on Instrumentation and Measurement*, vol. 56, no. 5, pp. 1648–1657, 2007.

[34] M. A. Platas-Garza and J. A. de la O Serna, "Dynamic Harmonic Analysis Through Taylor–Fourier Transform," *IEEE Transactions on Instrumentation and Measurement*, vol. 60, no. 3, pp. 804–813, 2011.

[35] D. Macii, A. Bashian, X. Shan, D. Fontanelli, H. Wen, and D. Petri, "Single-cycle P Class Phasor Estimation based on Harmonics Whitening and Off-nominal Frequency Offset Adjustment," *Electric Power Systems Research*, vol. 229, p. 110119, 2024.

[36] X. Shan, D. Macii, D. Petri, and H. Wen, "Enhanced IpD2FT-Based synchrophasor estimation for M Class PMUs through adaptive narrowband interferers detection and compensation," *IEEE Transactions on Instrumentation and Measurement*, vol. 73, pp. 1–14, 2024.

[37] P. Tosato, D. Macii, M. Luiso, D. Brunelli, D. Gallo, and C. Landi, "A tuned lightweight estimation algorithm for low-cost phasor measurement units," *IEEE Transactions on Instrumentation and Measurement*, vol. 67, no. 5, pp. 1047–1057, 2018.

[38] A. Singh, K. Al Jaafari, S. K. Parida, A. Al-Durra, H. H. Zeineldin, and E. F. El-Saadany, "Dynamic synchrophasor estimation algorithm using taylor weighted least square method with harmonic input model," *IEEE Transactions on Industry Applications*, vol. 59, no. 6, pp. 7417–7427, 2023.

[39] M. Radulović, Ž. Zečević, and B. Krstajić, "Dynamic phasor estimation by symmetric taylor weighted least square filter," *IEEE Transactions on Power Delivery*, vol. 35, no. 2, pp. 828–836, April 2020.

[40] M. Karimi-Ghartemani, "Synchronous reference frame PLL," in *Enhanced Phase-Locked Loop Structures for Power and Energy Applications*. John Wiley & Sons, Ltd, 2014, ch. 6, pp. 133–145.

[41] S. Golestan, J. M. Guerrero, and J. C. Vasquez, "Three-phase PLLs: A review of recent advances," *IEEE Trans. on Power Electronics*, vol. 32, no. 3, pp. 1894–1907, 2017.

[42] C. Hou, M. Zhu, Z. Li, and X. Cai, "Performance analysis of phase-locked loop based on third-order generalized integrator under inter-harmonic perturbation," in *2020 IEEE 9th Int. Power Electronics and Motion Control Conference (IPEMC2020-ECCE Asia)*, 2020, pp. 955–960.

[43] C. Zhang, X. Zhao, X. Wang, X. Chai, Z. Zhang, and X. Guo, "A grid synchronization PLL method based on mixed second-and third-order generalized integrator for DC offset elimination and frequency adaptability," *IEEE Journal of Emerging and Selected Topics in Power Electronics*, vol. 6, no. 3, pp. 1517–1526, 2018.

[44] P. Rodríguez, R. Teodorescu, I. Candela, A. V. Timbus, M. Liserre, and F. Blaabjerg, "New positive-sequence voltage detector for grid synchronization of power converters under faulty grid conditions," in *2006 37th IEEE Power Electronics Specialists Conf.*, 2006, pp. 1–7.

[45] M. Ciobotaru, R. Teodorescu, and F. Blaabjerg, "A new single-phase PLL structure based on second order generalized integrator," in *2006 37th IEEE Power Electronics Specialists Conference*, 2006, pp. 1–6.

[46] C. Muscas and P. Pegoraro, "Chapter 3 - algorithms for synchrophasors, frequency, and ROCOF," in *Phasor Measurement Units and Wide Area Monitoring Systems*, A. Monti, C. Muscas, and F. Ponci, Eds. Academic Press, 2016, pp. 21–51.

[47] R. Mittal, L. Fan, and Z. Miao, "Harmonic state-space model of second-order generalized integrator phase-locked loop," in *2021 IEEE Power & Energy Society General Meeting (PESGM)*, 2021, pp. 1–5.

[48] L. Feola, R. Langella, and A. Testa, "On the effects of unbalances, harmonics and interharmonics on PLL systems," *IEEE Transactions on Instrumentation and Measurement*, vol. 62, no. 9, pp. 2399–2409, 2013.

[49] EN 50160:2022, "Voltage characteristics of electricity supplied by public electricity networks," pp. 1–56, 2022.

[50] IEEE Std 519-2022 (Revision of IEEE Std 519-2014), "IEEE Standard for Harmonic Control in Electric Power Systems," pp. 1–31, 2022.

[51] F. Cecati, J. K. M. Becker, S. Pugliese, Y. Zuo, M. Liserre, and M. Paolone, "LTP modeling and analysis of frequency coupling in PLL-synchronized converters for harmonic power flow studies," *IEEE Transactions on Smart Grid*, vol. 14, no. 4, pp. 2890–2902, 2022.

[52] X. Wang and F. Blaabjerg, "Harmonic stability in power electronic-based power systems: Concept, modeling, and analysis," *IEEE Transactions on Smart Grid*, vol. 10, no. 3, pp. 2858–2870, 2019.